Published in final edited form as:
Med Phys. 2007 January ; 34(1): 221–232.

Computation of the glandular radiation dose in digital tomosynthesis of the breast

Ioannis Sechopoulos,
Emory University School of Medicine, Department of Radiology and Winship Cancer Institute, 1701 Uppergate Drive, Suite 5018, Atlanta, Georgia 30322 and Georgia Institute of Technology, Wallace H. Coulter Department of Biomedical Engineering, 313 Ferst Drive, Atlanta, Georgia 30332

Sankararaman Suryanarayanan,
Emory University School of Medicine, Department of Radiology and Winship Cancer Institute, 1701 Uppergate Drive, Suite 5018, Atlanta, Georgia 30322

Srinivasan Vedantham,
Emory University School of Medicine, Department of Radiology and Winship Cancer Institute, 1701 Uppergate Drive, Suite 5018, Atlanta, Georgia 30322

Carl D'Orsi, and
Emory University School of Medicine, Department of Radiology and Winship Cancer Institute, 1701 Uppergate Drive, Suite 5018, Atlanta, Georgia 30322

Andrew Karellas[a]
Emory University School of Medicine, Department of Radiology and Winship Cancer Institute, 1701 Uppergate Drive, Suite 5018, Atlanta, Georgia 30322 and Georgia Institute of Technology, Wallace H. Coulter Department of Biomedical Engineering, 313 Ferst Drive, Atlanta, Georgia 30332

Abstract

Tomosynthesis of the breast is currently a topic of intense interest as a logical next step in the evolution of digital mammography. This study reports on the computation of glandular radiation dose in digital tomosynthesis of the breast. Previously, glandular dose estimations in tomosynthesis have been performed using data from studies of radiation dose in conventional planar mammography. This study evaluates, using Monte Carlo methods, the normalized glandular dose (D_gN) to the breast during a tomosynthesis study, and characterizes its dependence on breast size, tissue composition, and x-ray spectrum. The conditions during digital tomosynthesis imaging of the breast were simulated using a computer program based on the Geant4 toolkit. With the use of simulated breasts of varying size, thickness and tissue composition, the D_gN to the breast tissue was computed for varying x-ray spectra and tomosynthesis projection angle. Tomosynthesis projections centered about both the cranio-caudal (CC) and medio-lateral oblique (MLO) views were simulated. For each projection angle, the ratio of the glandular dose for that projection to the glandular dose for the zero degree projection was

[a]Electronic mail: akarell@emory.edu.

computed. This ratio was denoted the relative glandular dose (RGD) coefficient, and its variation under different imaging parameters was analyzed. Within mammographic energies, the RGD was found to have a weak dependence on glandular fraction and x-ray spectrum for both views. A substantial dependence on breast size and thickness was found for the MLO view, and to a lesser extent for the CC view. Although RGD values deviate substantially from unity as a function of projection angle, the RGD averaged over all projections in a complete tomosynthesis study varies from 0.91 to 1.01. The RGD results were fit to mathematical functions and the resulting equations are provided.

Keywords

tomosynthesis; digital mammography; dosimetry; breast; Monte Carlo

I. INTRODUCTION

Tomosynthesis1–3 and dedicated computed tomography4–7 of the breast are being investigated as alternatives to conventional (planar) mammography, which suffers from the limitation of depicting three-dimensional information in a two-dimensional image, potentially resulting in an increase of false positives or missed cancers due to the inherent superposition of tissue.8,9 Digital tomosynthesis is a technique that enables tomographic imaging from a limited number of projections. Digital tomosynthesis of the breast was demonstrated by Niklason *et al.*2 in 1997, and since then several studies have been published on the subject. Suryanarayanan *et al.*10,11 compared several tomosynthesis reconstruction methods to planar mammography and found significantly better threshold contrast-detail characteristics in tomosynthesis phantom images. Wu *et al.* implemented a nonlinear iterative reconstruction method,12,13 and compared its performance to several other reconstruction methods.14 All these studies report that digital tomosynthesis has the ability to suppress the masking effect of superimposed structures.2,10–16

Given the promising results found in these studies, which point to the feasibility of clinical use of tomosynthesis of the breast, it has become imperative to characterize the radiation dose during a tomosynthesis acquisition. Current knowledge on radiation dose to the breast from digital tomosynthesis is limited, and any dose estimate must be made by using data computed for planar mammography. Although the radiation dose in planar mammography has been studied extensively,17–21 these studies characterize the breast as seen in a cranio-caudal view. Therefore, there is a need to evaluate the radiation dose to the breast glandular tissue during digital breast tomosynthesis examinations. For this, projection acquisitions centered about the medio-lateral oblique (MLO) view need to be considered,13 and the variation of glandular dose with projection angle must be characterized. This study's aim is to perform a comprehensive characterization of glandular dose to the breast tissue during a tomosynthesis study, taking into account the possible variations in breast size, composition, x-ray spectrum and mammographic view.

II. METHODS AND MATERIALS

We developed a C++ program, based on the Geant4 toolkit,22,23 that models image acquisition during a digital tomosynthesis exam of the breast. Geant4 is a set of C++ libraries which provide the functionality necessary to perform Monte Carlo based simulations of particle travel through matter. It is developed, supported and maintained by the Geant4 collaboration, a world-wide group of scientists and software engineers from various institutions.

In our simulations, one million mono-energetic x-rays were emitted from the simulated x-ray point source towards the detector, and the energy deposited by any photon interaction that took place in the breast tissue was recorded and used to calculate the mono-energetic normalized glandular dose [$D_gN(E)$] as described by Boone20 with the suggestions by Wilkinson and Heggie.24 This was repeated for all the different possible combinations of the values used for breast size, thickness and glandular fraction. For each combination the energy was varied from 5.5 to 35.5 keV in 1 keV steps, and the tomosynthesis projection angle was varied from 0° to ±30° in 3° steps [due to the geometrical symmetry, only the positive angles were used in the cranio-caudal (CC) view simulations]. Three degree steps were used because it was deemed that this gave sufficient data to perform an adequate interpolation for other angles. This resulted in a total of 173,600 runs each of one million photons. The simulations were performed on a 64 node computer cluster, each node containing two AMD Opteron 2.2 GHz processors (Advanced Micro Devices, Inc., Sunnyvale, CA). The $D_gN(E)$ results for each geometry and angle with 1 keV resolution were computer fit using commercially available software (TableCurve 2D, Systat Software Inc., Richmond, CA) to obtain 0.5 keV resolution. The mono-energetic $D_gN(E)$ results were combined with different simulated spectra25 relevant to mammographic applications as described by Thacker26 to obtain spectral D_gN coefficients. For this study the spectra used are listed in Table I, along with their first half-value layers (HVLs), specified in mm of Al, as would be measured experimentally (under the breast compression plate), and as used for the computations (before the breast compression plate). This difference arises from the fact that the breast compression plate was included in the Monte Carlo simulations.

The acquisition system model included the full-field detector, detector cover, breast support plate, and breast compression plate. The x-ray source was modeled as a point source located at the chest-wall side edge of the detector, with its center of rotation (COR) located 4 cm above the detector surface. The source's distance from the COR was 62 cm. This results in a source-to-imager distance of 66 cm at a tomosynthesis angle of 0°. An air gap of 1.5 cm between the detector cover and the breast support plate was included. The tomosynthesis angle α was defined as measured at the detector surface, not at the COR. Given the tomosynthesis angle measured at the detector surface (α), the tomosynthesis angle measured from the COR (β) can be computed from:

$$\beta = \alpha + \arcsin\left(\frac{l \times \sin(\alpha)}{h}\right), \quad (1)$$

where l is the distance from the detector surface to the COR (4 cm in this study), and h is the distance from the COR to the x-ray source (62 cm) (Fig. 1).

The x-ray field from the source was collimated so that it was exactly congruent with the detector's active area. This involved modeling the collimation as variable with projection angle to maintain the x-ray field within the limits of the detector area at all angles. This variable collimation is necessary due to the fact that the detector remains stationary while the x-ray source rotates. The heel effect was included in the simulation, so the x-ray intensity was highest at the central ray, dropping to lower intensities away from it. To determine the correct x-ray intensity drop off due to the heel effect and the inverse square distance relationship, the variation in exposure at different locations above the detector surface of a clinical digital mammography unit (GE Senographe 2000D, GE Healthcare, Waukesha, WI) was measured using a calibrated dosimeter with a mammography ionization chamber (Radcal Corp., Monrovia, CA). Measurements were performed at 26 and 30 kVp, and the results were imported into the Monte Carlo simulation.

In this study, the D_gN for the zero degree projection angle (D_gN_0) only is reported. For the nonzero projection angles, the value reported is the relative glandular dose coefficient [RGD(α)], which describes the ratio of the glandular dose for that projection to the glandular dose for the zero degree projection while maintaining the kVp and mAs setting constant. The D_gN_0 is reported in units of dose to the breast per unit exposure at a specific point, in milliGray per Roentgen. This specific point is where the central ray meets the breast support plate, and the exposure is measured when no breast is present (Fig. 2). This exposure reference point allows the clinician or medical physicist to have a pre-measured table of exposures at the reference point for the different imaging techniques (in terms of target and filter material and kVp setting) independently of the breast imaged. Although D_gN is typically reported as dose per unit entrance skin exposure, for this study a different exposure reference point was introduced due to the inclusion of the heel effect and inverse square distance relationship in the simulation and the complexity of the breast shape in the MLO view, which make the entrance skin exposure difficult to measure. In contrast, the exposure at the intersection of the central ray and the breast support plate is easily measured and it is constant for the same x-ray beam quality (kVp and HVL) and mAs settings. The use of RGD(α) was chosen due to the difficulty of locating consistently on the detector surface the point of equal exposure while the x-ray tube is rotating.

For the reported data, the total glandular dose for a tomosynthesis study is given by:

$$\begin{aligned} D_g &= X_{\mathrm{CR}} \times D_gN_0 \times \sum_{\alpha=\alpha_{\mathrm{MIN}}}^{\alpha_{\mathrm{MAX}}} \mathrm{RGD}(\alpha) \\ &= X_{\mathrm{CR}} \times D_gN_0 \times N_\alpha \times \mu_{\mathrm{RGD}}, \end{aligned} \quad (2)$$

where D_g is the total glandular dose, in mGy; X_{CR} is the exposure measured at the reference point with the x-ray tube at the zero degree projection position (Fig. 2) for the kVp and mAs setting used in the study, in R; D_gN_0 is the normalized glandular dose for the zero degree projection (reported here), in mGy per R; RGD(α) is the relative glandular dose coefficient (reported here), which is unitless; N_α is the number of projections in the study; and μ_{RGD} is

the mean RGD over all angles. The summation is performed over all the angles used in the tomosynthesis study (including the zero degree angle, which by definition has a RGD of 1).

A. Simulation geometry details

Although it is possible that only projections centered about the MLO view will be used if tomosynthesis of the breast is performed routinely,13 the CC view was also studied.

The breast in MLO view was simulated as a complex solid which included a portion of the pectoralis muscle (Fig. 3), since it is normally present in a clinical MLO view image. The superior portion of the pectoralis muscle and the breast tissue that is included in the image is located towards the top edge of the image for all breast sizes because in the MLO view the corner of the detector is positioned posterior to the patient's axilla.27 This means that for small breasts, most of the tissue will be located off center towards the superior side of the image.

The breast is varied using three parameters: chest-wall to nipple distance (CND), compressed breast thickness (T), and glandularity (G). The CND was defined as the distance from the detector edge to the point in the breast skin farthest away from the body. With varying CND, the length of the breast along the chest wall and the size of the pectoralis were made to vary proportionally. In this study, the CND was varied from 7 to 19 cm, in steps of 3 cm, while the thicknesses used ranged from 2 to 8 cm, in 1 cm steps. The glandularity was defined as the weight fraction of the breast that consists of glandular tissue and was set to 1, 25, 50, 75, and 100%. The composition of the glandular and adipose tissues were defined as described by Hammerstein *et al.*28 The composition of the pectoralis was specified as that of skeletal muscle according to the International Commission on Radiation Units and Measurements' Report 44.29 For both views, the breast tissue was surrounded by a 4 mm layer of skin, and for backscatter purposes, the patient's body was included in the simulation, modeled as a large cuboid of water (75×34×17 cm).

The compressed breast in CC view was simulated as a semicircle with rounded edges, located at the centerline of the imager (Fig. 4). The breast was defined using the same three parameters, CND, T and G. Since in this view the breast was modeled as a semicircle, the CND defines the radius of the semicircle. The values for thickness and glandularity used were the same as those for the MLO view, while the CND was set so that the mass of the breast tissue coincided with that of the MLO view simulations' breast tissue mass, not including the pectoralis muscle. To match the breast mass, Geant4's function for calculation of the simulated breast tissue mass was used. Therefore, the CND values were: 6.2, 9.0, 11.6, 14.4, 17.0 cm.

B. Validation

To verify the photon attenuation coefficients used by Geant4 and the correct behavior of the simulation code, the program was modified so as to simulate x-rays traveling through breast tissue only, and the resulting attenuation coefficients were calculated. By activating and deactivating the different relevant physical interaction processes (photoelectric effect,

Compton and Rayleigh scattering) in the Geant4 program, the linear attenuation coefficients of each process could be verified. These data were compared with the literature.28,30

The simulation was also validated by comparing, under similar conditions, the values obtained for the zero degree projection against those reported by Wu *et al.*18,19 and by Boone21 for planar mammography. This involved modifying the Monte Carlo simulation so that the geometry matched as closely as possible to that reported by the authors. In addition, the simulation was modified so that the x-ray field was limited to the compressed breast, not the whole imager. To perform a valid comparison, the resulting data were also referenced to the entrance skin exposure, by performing the x-ray fluence to exposure conversion in a similar fashion as that reported by the authors.

III. RESULTS

To verify that one million photon runs achieved enough statistical precision, the geometry in which the smallest number of photons would interact with the breast was repeated five times and the variation analyzed. The geometry used was that given by a CND of 7 cm and a thickness of 2 cm in the MLO view, and the coefficient of variation (defined as the percentage ratio of standard deviation to the mean, COV=$100\sigma/\mu$)of the resulting D_gN values was found to be 0.47%.

A. Validation results

Figures 5 and 6 show the linear attenuation coefficients calculated from Geant4's simulations compared to the data reported by Hammerstein *et al.*28 for breast tissue, and the decomposed linear attenuation coefficients compared to XCOM's database.30 In both cases excellent agreement was found. Figure 7 shows the D_gN values obtained from the Geant4 simulation compared to the data of Wu *et al.*18 and Boone21 for matching geometries and compositions, respectively. In both cases good agreement was observed with excellent correlation (r^2>0.998 and r^2>0.999, respectively).

B. Normalized glandular dose at zero degree projection angle

Table II shows the computed normalized glandular doses for the zero degree projection angle, D_gN_0, as a function of compressed breast thickness, glandularity, and x-ray spectrum for the MLO and CC views. Although in this study D_gN_0 was computed for breasts with different chest-wall to nipple distances, D_gN_0 was found to be very similar with varying CND, so the data reported here, due to space constraints, is the mean D_gN_0 for the five CND values simulated.

For the MLO view, the D_gN_0 for the CND=7 cm case is approximately 6%–14% lower than the values reported in Table II, while for breasts with CND of 10 cm or larger the reported D_gN_0 is accurate to within 6%. For the CC view, the maximum deviation from the mean D_gN_0 presented here is 3% for all breast sizes. For both views, as expected, increasing spectrum energy has a proportional effect on D_gN_0, while increasing thickness and glandularity show an inversely proportional relationship.

C. Relative glandular dose coefficients in MLO view

The RGD for all the geometries, glandularities and spectra used in this study were analyzed to find the effect each parameter has on RGD. For the MLO case, it was found that glandularity and spectrum have a weak effect on the values of RGD, while, as expected, CND and *T* show a very important effect (example graphs are shown in Fig. 8). To quantify the impact of glandularity and spectrum, the variation of RGD when varying each one of these parameters while keeping all the other variables constant was computed using the COV and the percent deviation from the mean (DFM=100 ×|RGD−μ|/μ) as the selected metrics. The results are shown in Table III. The sensitivity of RGD to varying breast size and thickness shown by the variation metrics can be also seen in Figs. 8(c) and 8(d), which show that increasing breast size substantially changes the effect of projection angle on RGD, while increasing thickness increases the slope of RGD with tomosynthesis angle. Due to the position and geometry of the breast in the MLO view, changes in breast size vary the relative location of most of the breast tissue on the detector. These displacements in breast tissue are what introduce the variations in the RGD distribution with projection angle observed in Fig. 8(c).

The computed RGD was computer fit to functions of CND and angle, resulting in an equation for a surface for each thickness simulated. For simplicity, the RGD values were fit to the same equation for all *T* values, resulting in only different coefficients for each fit. The surface fits were performed using commercially available software (Table-Curve 3D, Systat Software Inc., Richmond, CA), and all seven fits resulted in an r^2>0.994. The equation for RGD for the MLO view is of the form:

$$\mathrm{RGD}_{\mathrm{MLO}}=\frac{a+c\alpha+e\delta+g\alpha^2+i\delta^2+k\alpha\delta}{1+b\alpha+d\delta+f\alpha^2+h\delta^2+j\alpha\delta}, \quad (3)$$

where α is the tomosynthesis angle (measured from the detector surface), in degrees; is the compressed breast chest-wall to nipple distance, in cm; and *a* through *k* are the fit coefficients, given in Table IV.

D. Relative glandular dose coefficients in CC view

A similar analysis was performed with the RGD data computed for the CC view (example graphs are shown in Fig. 9). A weak dependence on glandularity and spectrum was found for RGD, while thickness and chest-wall to nipple distance showed a much smaller effect on RGD in the CC view than in the MLO view. The results for the CC view are also shown in Table III. The variation of RGD with *T* and CND were still deemed important enough so as to not fit RGD as only a function of projection angle. Therefore, the RGD values for CC view were also surface fitted (r^2 >0.995), using the same software, resulting in an equation for all seven thicknesses of the form:

$$\begin{aligned}\mathrm{RGD}_{CC}=a+b\alpha+c\delta+d\alpha^2+e\delta^2+f\alpha\delta+g\alpha^3+h\delta^3\\+i\alpha\delta^2+j\alpha^2\delta,\end{aligned} \quad (4)$$

where the parameters are the same as those for the MLO fit, and the fit coefficients *a* through *j* are also specified in Table IV.

IV. DISCUSSION

Comparison of D_gN_0 between the MLO and CC views shows that an MLO acquisition imparts a lower normalized glandular dose than a CC acquisition, by as much as 11%. This could be attributed to the fact that in the CC view model, the breast tissue is located around the central ray, where the photon fluence is highest. In the MLO view, the breast is located towards one side of the detector, where, due to the heel effect and inverse square distance relationship, the photon fluence is decreased. Also, more importantly, the pectoralis muscle present in the MLO view absorbs a portion of the dose that would otherwise be absorbed by the breast tissue. The presence of the pectoralis muscle in the compressed breast acts as a shield for the breast tissue under it, resulting in a lower total dose to the breast tissue. The energy deposited in the muscle tissue was found to range from 1.5% to 12% of that deposited in the breast tissue, varying inversely with breast thickness. When a breast is compressed in the MLO position it is almost always of greater thickness than when it is compressed in the CC position.31,32 Therefore, for MLO view images a higher exposure is used than for CC view images, resulting in a higher total dose even though the D_gN_0 is lower.

Given the definition of RGD(α), if the mean RGD, μ_{RGD}, of a complete tomosynthesis study is under 1, then the study will result in a lower total glandular dose than a planar mammography study, if the mAs setting for all the projections in the tomosynthesis study is constant and the sum of the mAs used equals that of the planar study. Similarly, if μ_{RGD} is over 1, the tomosynthesis study will result in a higher glandular dose than the equivalent planar study. If in an advanced tomosynthesis system the mAs is adjusted for each projection, this can be taken into account by incorporating the increase at each angle into Eq. (2). Furthermore, if the kVp setting is also varied with angle, then the total dose of the study can also be computed by multiplying each angle's coefficient by its corresponding D_gN_0 and then totaling the normalized glandular doses.

Using the tomosynthesis protocol reported for a current prototype tomosynthesis system33 (21 views over an angular range of $\alpha = \pm 30°$, in 3° steps), μ_{RGD} can be calculated for different breast parameters. For all the sets of possible parameter values (1575 combinations) used in this study in the MLO view the maximum μ_{RGD} for the protocol described above is 1.01, while the minimum is 0.91. For the CC view the maximum and minimum μ_{RGD} are 0.97 and 0.91, respectively. This means that for the tomosynthesis protocol described, conventional mammography dosimetry could overestimate the dose to the breast by almost 10% for both views. This seemingly small deviation from unity of μ_{RGD} is not due to the individual RGD(α) values being always close to unity. In the cases where the RGD(α) deviates considerably from unity, the RGD(α) distribution's approximate negative symmetry about 1 [RGD($-\alpha$) =1− (RGD(α) −1)] still results in a μ_{RGD} of approximately 1 [Fig. 10(a)]. Specifically, for the breast with CND=7 cm and T=8 cm, the extreme individual RGD(α) values are 0.44–1.47, but the resulting μ_{RGD} is 1.0. In the MLO views where CND is large (e.g., CND =19 cm, T=8 cm), RGD(α) has a distribution which is approximately positive symmetric [RGD($-\alpha$) =RGD(α)] about the zero degree projection angle, resulting in a μ_{RGD} of 0.92 [Fig. 10(b)]. Therefore, in this case, the total glandular dose to the breast during a tomosynthesis study will be 8% lower than that of a planar

mammography study performed with equal total mAs. In addition, it must be noted that a small breast results in a higher μ_{RGD} than that for a large breast. The CC view with large CND results in approximately the same μ_{RGD} as that of the MLO view.

In case that some small breasts are placed in the center of the detector for the MLO view rather than towards the superior side, some simulations were repeated to study this positioning. Using a small breast of varying thickness (CND =10 cm, T=2, 5, and 8 cm, G=50%) with the MLO view shape but positioned about the centerline of the imager, simulations were performed for the ±30° range in 3° steps, and the resulting RGD(α) was computed. The results for the T=5 cm case are displayed in Fig. 11. As can be seen from the graph, the RGD(α) for the MLO view breast, when centered on the detector, presents a very similar distribution with projection angle to that of the CC view of equivalent mass. Similar results were found for the breasts with T=2 and 8 cm. Therefore, the fit equation for RGD(α) for the CC view could be used to compute doses for MLO view breasts positioned in this manner. These results are expected since the small size of the breast makes the difference in shape relatively unimportant.

A simulation with a median geometry (CND=13 cm, T =5 cm, G=50%) was repeated without taking into account the heel effect in the x-ray field distribution. Therefore, the only nonuniformity present in the x-ray fluence was due to the divergence of the x rays from the point source, which follows the inverse square law. As expected, it was found that the removal of the heel effect has a substantial effect in the D_gN_0 values, which increased by approximately 7% for all spectra, while the RGD(α) was minimally affected, the variation ranging from 0% to 0.5%, with a mean variation of 0.14%.

Additional simulations were performed with two different values for the distance from the detector surface to the x-ray tube's center of rotation (DCOR), originally 4 cm in this study. This distance was specified as 0 cm (center of rotation at the detector surface) and 8 cm above the detector surface. The source to detector distance at the zero degree projection angle was maintained at 66 cm. Simulations with these two values for DCOR were performed for CND=13 cm for MLO view (11.6 cm for CC view), T=2, 5 and 8 cm and G =50%. For both views the RGD(α) was found to be directly proportional with DCOR, having lower values compared to the original study's data with DCOR=0 cm and higher with DCOR=8 cm (Fig. 12). For the MLO view, the values for RGD(α) varied by a maximum at the extreme angles of approximately 5%, while for the CC view the maximum deviations were found to be of approximately 2%, both in relation to the values found for the original study of DCOR=4 cm. These results could be explained by the fact that a higher center of rotation results in a shorter distance from the x-ray source to the compressed breast at nonzero projection angles compared to the distance for a lower center of rotation. Therefore, since the x-ray source is closer to the compressed breast, the relative glandular dose is higher.

These additional simulations show that the tables and equations reported in this study are approximately valid for tomosynthesis systems with some deviations, such as different x-ray fluence nonuniformities and different locations of the x-ray tube's center of rotation. However, this study is not necessarily applicable to tomosynthesis projection geometries in

which the detector rotates in conjunction with the x-ray tube. This limitation is especially true for the MLO view dose simulations, for which some of the breast tissue falls outside the x-ray field at certain tomosynthesis projection angles. These results would be applicable for small to medium sized breasts in the CC view, for which the whole breast is always within the x-ray field.

V. CONCLUSION

Conventional mammographic dosimetry was not designed to address the complex geometry of tomosynthesis projections. In this study, we have found that geometric asymmetry, specific characteristics of the MLO view, varying x-ray field collimation, and inclusion of the heel effect result in a complex variation of normalized glandular dose with projection angle. For a complete tomosynthesis acquisition, the normalized glandular dose to the breast, when computed with conventional dosimetry was found to be overestimated by as much as approximately 10%. Although this percentage difference might be deemed unimportant compared to the errors introduced by the necessary approximations of this type of simulation (breast geometry variations, tissue inhomogeneities, etc.), it is important to note that for some projection angles the deviation was found to be as much as 56%, which could introduce important deviations if advanced tomosynthesis protocols, such as varying mAs with projection angle, are introduced.

This new model of dosimetry can be used for a more realistic and accurate characterization of the normalized glandular dose in digital tomosynthesis of the breast than that obtained from the conventional mammography models. This model allowed for a comprehensive characterization of the parameters involved in tomosynthesis dosimetry, giving insight into which imaging and geometric parameters are important to consider when performing a tomosynthesis dosimetry calculation.

Acknowledgments

The authors would like to thank Steve Pittard for providing technical assistance with the use of Emory University's High Performance Computer Cluster. This study was supported in part by the National Institute of Health (NIH) Grant No. RO1-EB002123 from the National Institute of Biomedical Imaging and Bioengineering (NIBIB). This work was also supported by a grant from the Georgia Cancer Coalition (GCC). The contents are solely the responsibility of the authors and do not necessarily represent the official views of the NIH, NIBIB or the GCC.

References

1. Kolitsi Z, Panayiotakis G, Anastassopoulos V, Scodras A, Pallikarakis N. A multiple projection method for digital tomosynthesis. Med Phys. 1992; 19:1045. [PubMed: 1518466]
2. Niklason LT, et al. Digital tomosynthesis in breast imaging. Radiology. 1997; 205:399–406. [PubMed: 9356620]
3. Dobbins JT III, Godfrey DJ. Digital x-ray tomosynthesis: Current state of the art and clinical potential. Phys Med Biol. 2003; 48:R65. [PubMed: 14579853]
4. Boone JM, Nelson TR, Lindfors KK, Seibert JA. Dedicated breast CT: Radiation dose and image quality evaluation. Radiology. 2001; 221:657–667. [PubMed: 11719660]
5. Ning R, Conover DL, Chen B, Schiffhauer L, Cullinan J, Ning Y, Robinson AE. Flat-panel-detector-based cone-beam volume CT breast imaging: Phantom and specimen study. Proc SPIE. 2002; 4682:218–227.

6. Chen B, Ning R. Cone-beam volume CT breast imaging: Feasibility study. Med Phys. 2002; 29:755–770. [PubMed: 12033572]
7. Gong X, Glick SJ, Liu B, Vedula AA, Thacker S. A computer simulation study comparing lesion detection accuracy with digital mammography, breast tomosynthesis, and cone-beam CT breast imaging. Med Phys. 2006; 33:1041–1052. [PubMed: 16696481]
8. Tabar L, Fagerberg G, Chen HH, Duffy SW, Smart CR, Gad A, Smith RA. Efficacy of breast cancer screening by age. New results from the Swedish Two-County Trial. Cancer. 1995; 75:2507–2517. [PubMed: 7736395]
9. Rosenberg RD, Lando JF, Hunt WC, Darling RR, Williamson MR, Linver MN, Gilliland FD, Key CR. The New Mexico Mammography Project. Screening mammography performance in Albuquerque, New Mexico, 1991 to 1993. Cancer. 1996; 78:1731–1739. [PubMed: 8859186]
10. Suryanarayanan S, Karellas A, Vedantham S, Glick SJ, D'Orsi CJ, Baker SP, Webber RL. Comparison of tomosynthesis methods used with digital mammography. Acad Radiol. 2000; 7:1085–1097. [PubMed: 11131053]
11. Suryanarayanan S, Karellas A, Vedantham S, Baker SP, Glick SJ, D'Orsi CJ, Webber RL. Evaluation of linear and nonlinear tomosynthetic reconstruction methods in digital mammography. Acad Radiol. 2001; 8:219–224. [PubMed: 11249085]
12. Wu T, et al. Tomographic mammography using a limited number of low-dose cone-beam projection images. Med Phys. 2003; 30:365–380. [PubMed: 12674237]
13. Wu T, Zhang J, Moore R, Rafferty E, Kopans D, Meleis W, Kaeli D. Digital tomosynthesis mammography using a parallel maximum-likelihood reconstruction method. Proc SPIE. 2004; 5368:1–11.
14. Wu T, Moore RH, Rafferty EA, Kopans DB. A comparison of reconstruction algorithms for breast tomosynthesis. Med Phys. 2004; 31:2636–2647. [PubMed: 15487747]
15. Stevens GM, Fahrig R, Pelc NJ. Filtered backprojection for modifying the impulse response of circular tomosynthesis. Med Phys. 2001; 28:372–380. [PubMed: 11318319]
16. Stevens GM, Birdwell RL, Beaulieu CF, Ikeda DM, Pelc NJ. Circular tomosynthesis: Potential in imaging of breast and upper cervical spine—preliminary phantom and in vitro study. Radiology. 2003; 228:569–575. [PubMed: 12821770]
17. Dance DR. Monte Carlo calculation of conversion factors for the estimation of mean glandular breast dose. Phys Med Biol. 1990; 35:1211–1219. [PubMed: 2236205]
18. Wu X, Barnes GT, Tucker DM. Spectral dependence of glandular tissue dose in screen-film mammography. Radiology. 1991; 179:143–148. [PubMed: 2006265]
19. Wu X, Gingold EL, Barnes GT, Tucker DM. Normalized average glandular dose in molybdenum target-rhodium filter and rhodium target-rhodium filter mammography. Radiology. 1994; 193:83–89. [PubMed: 8090926]
20. Boone JM. Glandular breast dose for monoenergetic and high-energy x-ray beams: Monte Carlo assessment. Radiology. 1999; 213:23–37. [PubMed: 10540637]
21. Boone JM. Normalized glandular dose (DgN) coefficients for arbitrary x-ray spectra in mammography: Computer-fit values of Monte Carlo derived data. Med Phys. 2002; 29:869–875. [PubMed: 12033583]
22. Agostinelli S, et al. Geant4—a simulation toolkit. Nucl Instrum Methods Phys Res A. 2003; 506:250.
23. Allison J, et al. Geant4 developments and applications. IEEE Trans Nucl Sci. 2006; 53:270–278.
24. Wilkinson L, Heggie JCP. Glandular breast dose: Potential errors. Radiology. 2001; 213:1.
25. Boone JM, Fewell TR, Jennings RJ. Molybdenum, rhodium, and tungsten anode spectral models using interpolating polynomials with application to mammography. Med Phys. 1997; 24:1863. [PubMed: 9434969]
26. Thacker SC, Glick SJ. Normalized glandular dose (DgN) coefficients for flat-panel CT breast imaging. Phys Med Biol. 2004; 49:5433–5444. [PubMed: 15724534]
27. Hendrick, RE., et al. Mammography Quality Control Manual. American College of Radiology; Reston, VA: 1999.

28. Hammerstein GR, Miller DW, White DR, Masterson ME, Woodard HQ, Laughlin JS. Absorbed radiation dose in mammography. Radiology. 1979; 130:485–491. [PubMed: 760167]

29. International Commission on Radiation Units and Measurements. Tissue Substitutes in Radiation Dosimetry and Measurement. International Commission on Radiation Units and Measurements; Bethesda, Md: 1989.

30. M. J. Berger, J. H. Hubbell, S. M. Seltzer, J. Chang, J. S. Coursey, R. Sukumar, and D. S. Zucker, (NIST, 2005), Vol. 2006.

31. Young KC, Burch A. Radiation doses received in the UK Breast Screening Program in 1997 and 1998. Br J Radiol. 2000; 73:278–287. [PubMed: 10817044]

32. Jamal N, Ng KH, McLean D. A study of mean glandular dose during diagnostic mammography in Malaysia and some of the factors affecting it. Br J Radiol. 2003; 76:238–245. [PubMed: 12711643]

33. Eberhard JW, et al. High-speed large-angle mammography tomosynthesis system. Proc SPIE. 2006; 6142:61420C–61411.

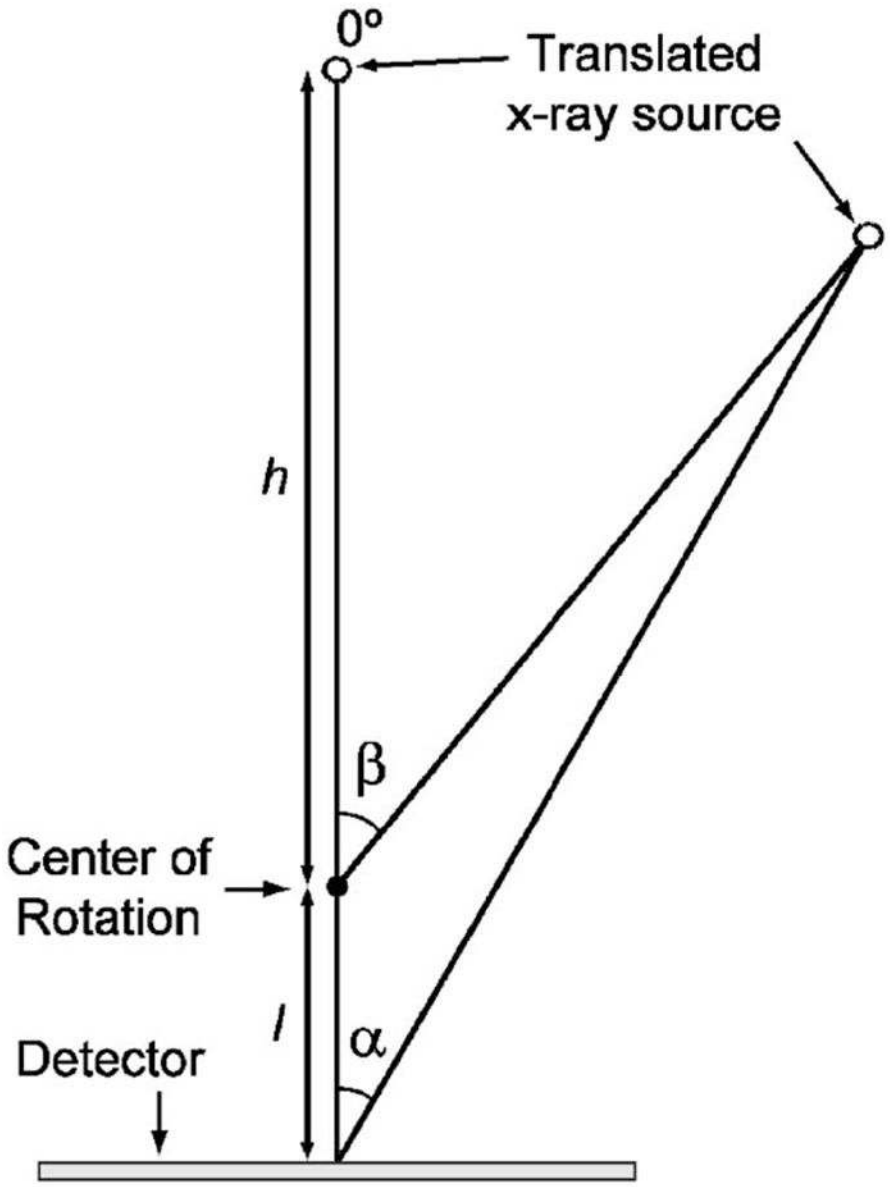

Fig. 1.

Diagram specifying the measurement location of the two projection angles related by Eq. (1).

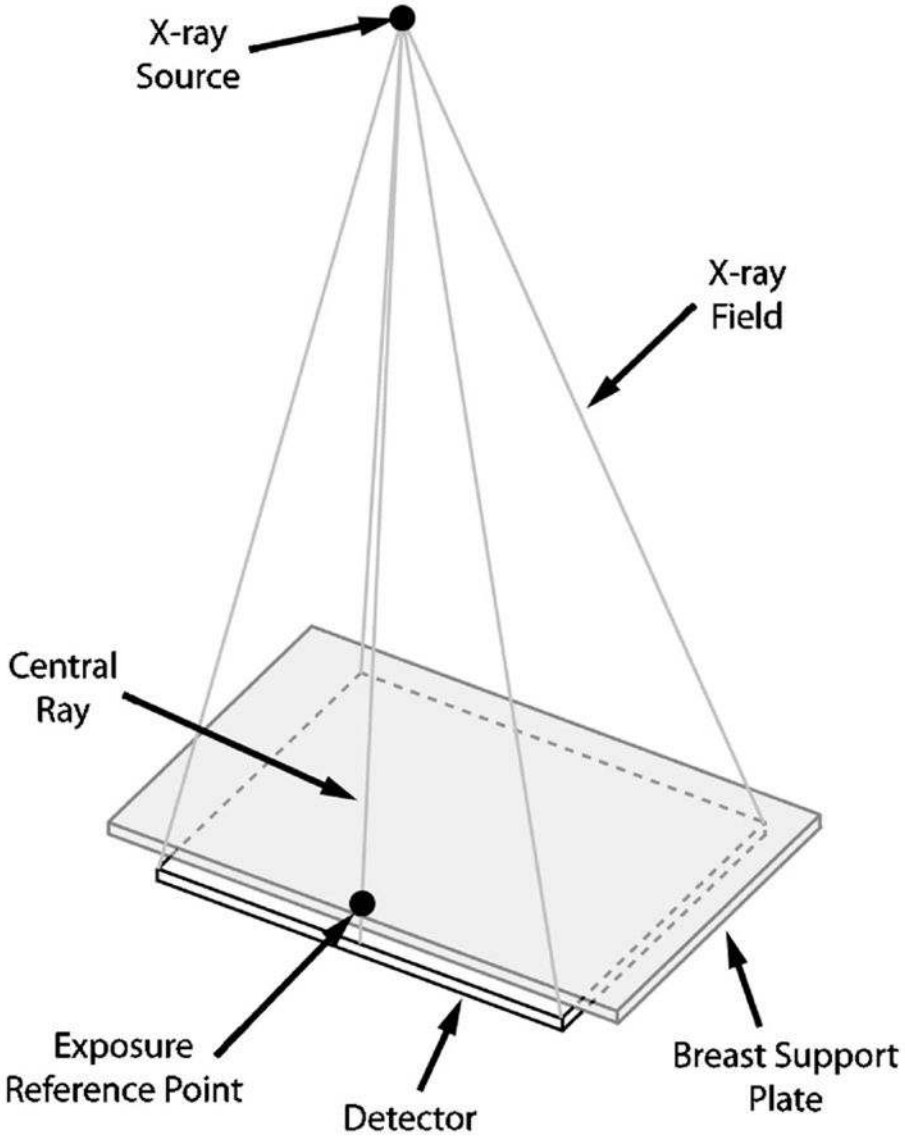

Fig. 2.

Diagram specifying the location to which the unit exposures in the normalized glandular dose values are referenced.

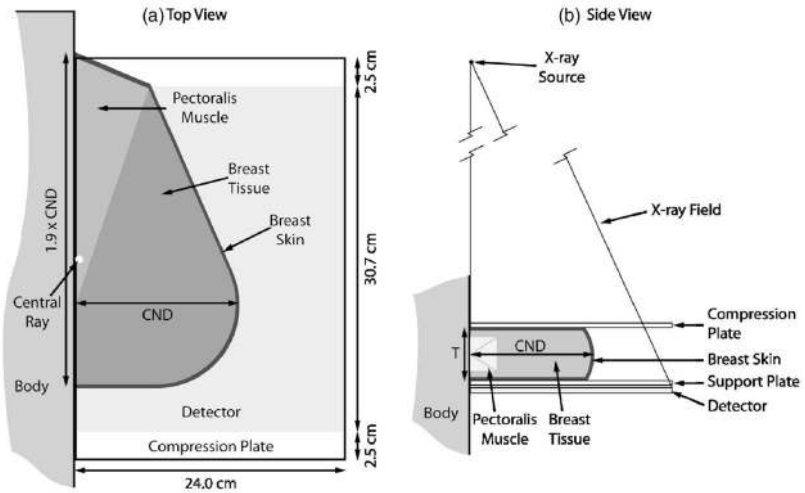

Fig. 3.

Diagram of the simulated MLO view. (a) Top view, (b) Side view. The pectoralis muscle's thickness decreases towards the caudal side. The length of the pectoralis muscle along the chest wall varies so that the lower edge aligns horizontally with the nipple. CND=chest-wall to nipple distance, *T*=compressed breast thickness.

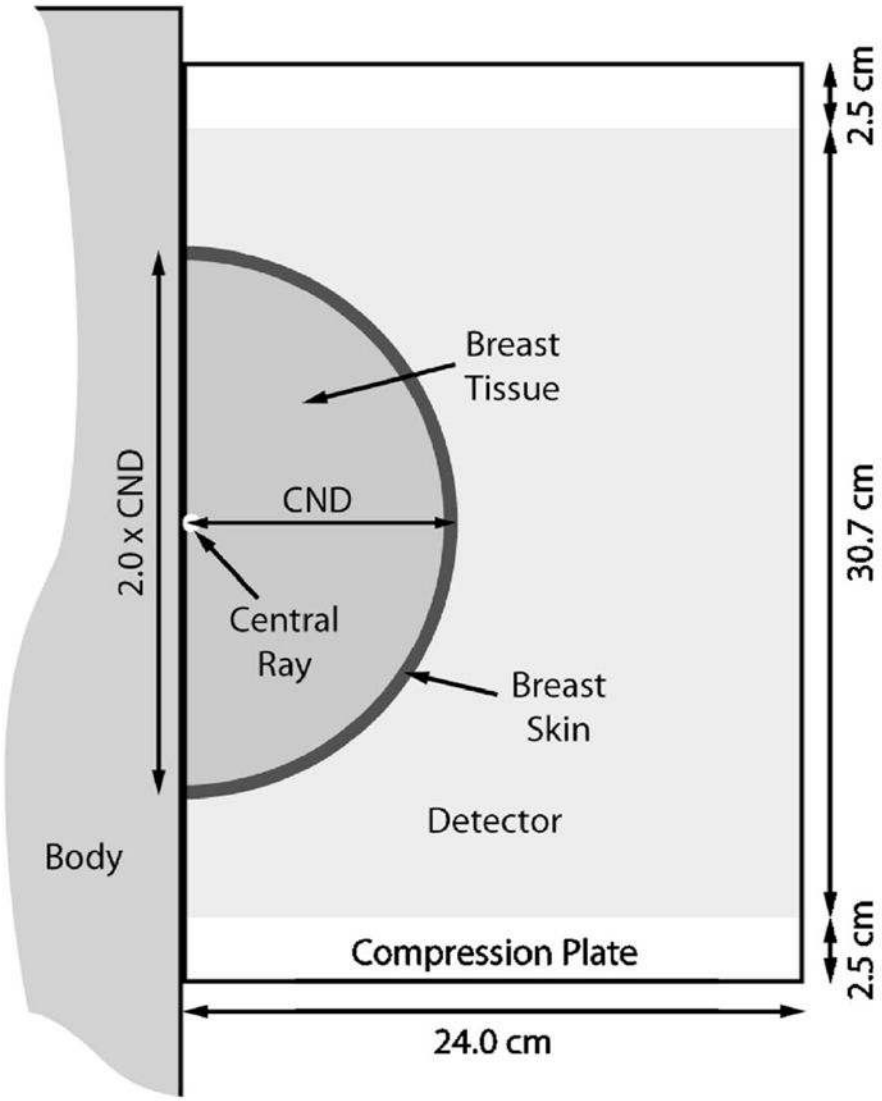

Fig. 4.

Diagram of the simulated CC view. CND=chest-wall to nipple distance, *T*=compressed breast thickness.

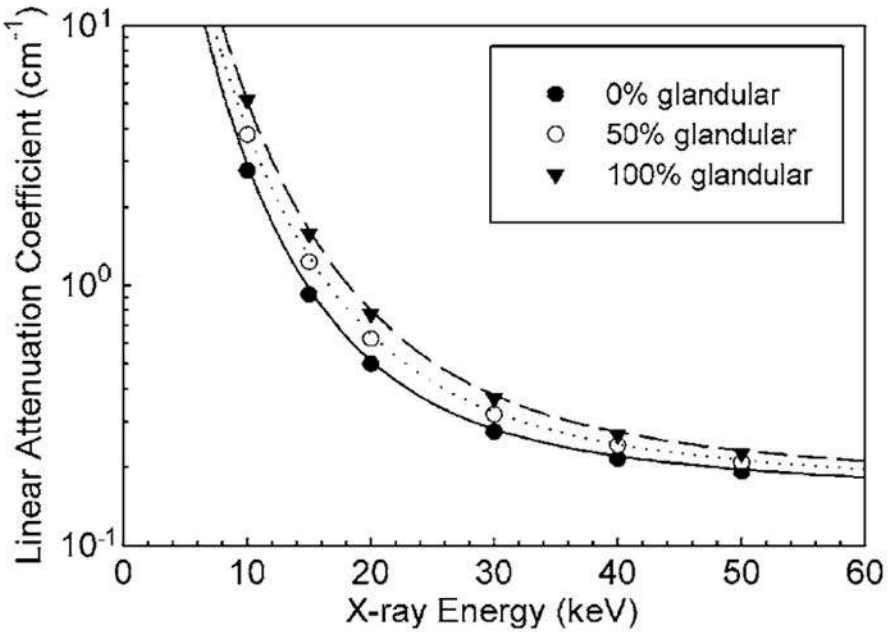

Fig. 5.

Comparison of the linear attenuation coefficients reported by Hammerstein *et al.* (Ref. 28) (symbols) and those resulting from the developed Geant4 program (lines). Excellent agreement can be seen for all three glandular fractions.

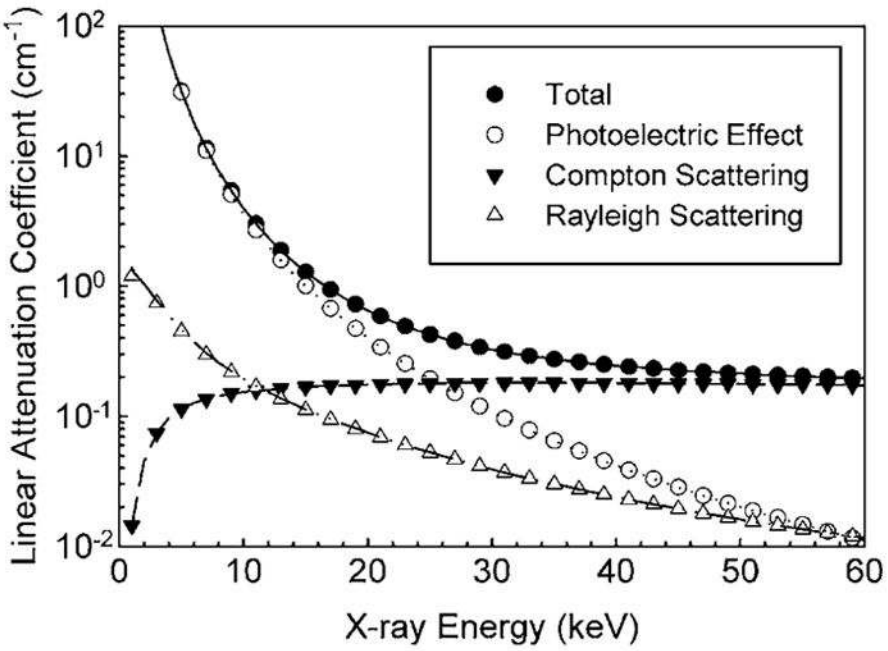

Fig. 6.

Total linear attenuation coefficients and their decomposition into the three relevant physical interaction processes for the simulated breast tissue with 50% glandular fraction. The symbols are National Institute of Standards and Technology's XCOM data (Ref. 30) and the lines show the data obtained from the developed Geant4 program. Similar agreement was found for the 100% adipose and the 100% glandular breast tissues.

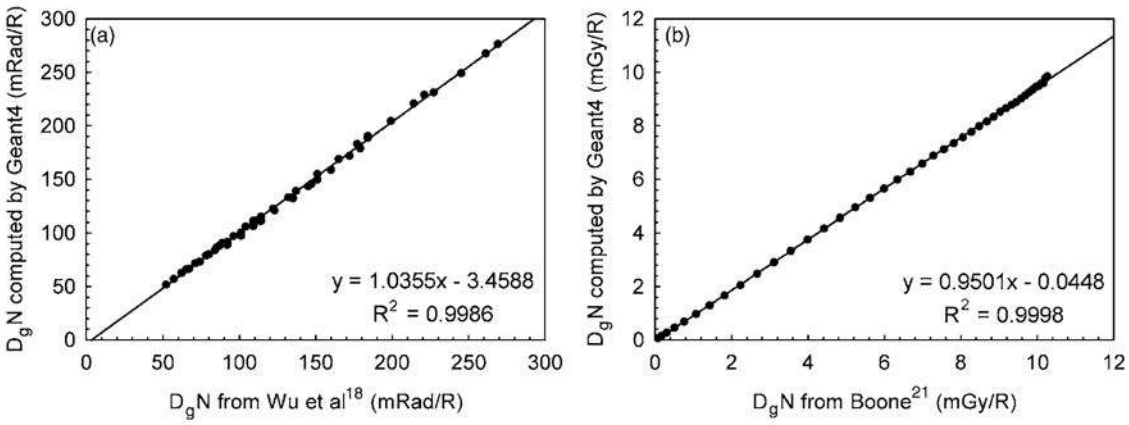

Fig. 7.

Comparison of D_gN values computed by the Geant4 program against those previously reported by (a) Wu *et al.* (Ref. 18) and (b) Boone (Ref. 21). The lines represent the linear fit that result in the displayed equations. Excellent agreement is observed in both cases.

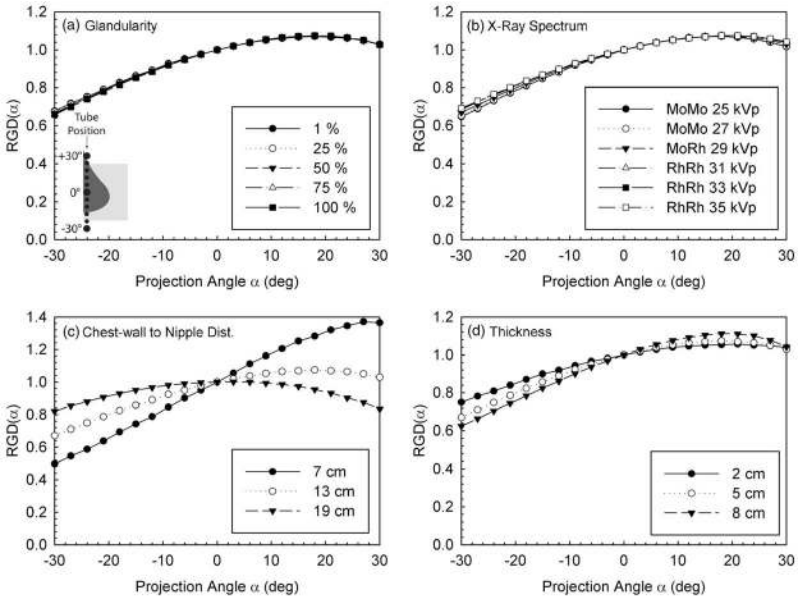

Fig. 8.

Sample graphs of RGD variation with varying (a) breast glandular fraction, (b) x-ray spectrum, (c) chest-wall to nipple distance, (d) compressed breast thickness. All four graphs are for MLO view, CND=13 cm, *T*=5 cm, *G*=50% and Mo-Rh 29 kVp x-ray spectrum, unless specified otherwise. Positive angle projections are defined as when the x-ray tube swings towards the cranial side of the patient. Note the different *Y*-axis scale in Fig. 8(c).

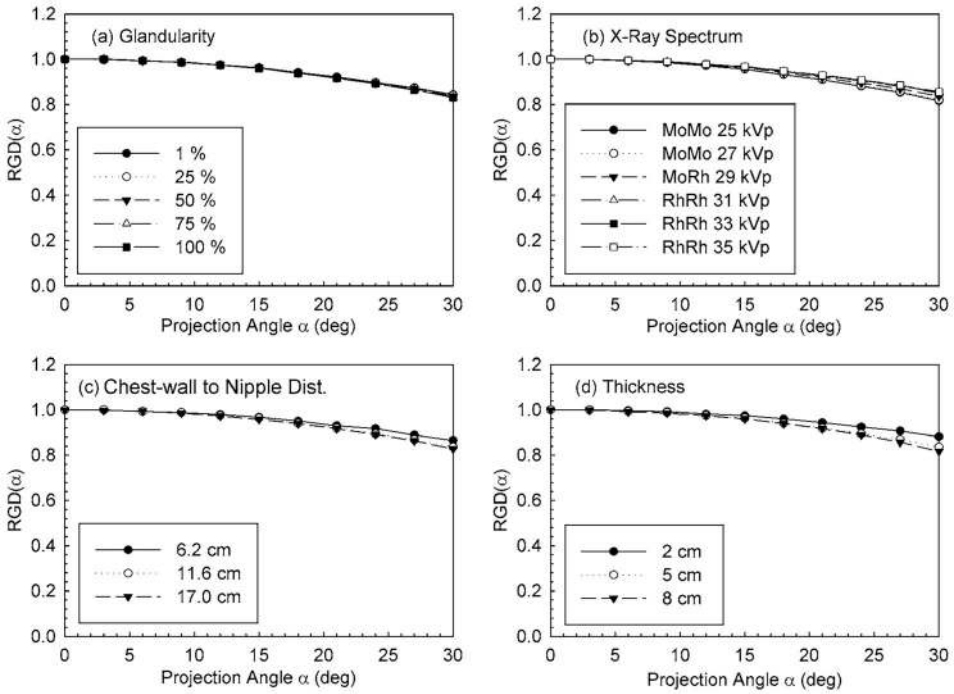

Fig. 9.

Sample graphs of RGD variation with varying (a) breast glandular fraction, (b) x-ray spectrum, (c) chest-wall to nipple distance, (d) compressed breast thickness. All four graphs are for CC view, CND=11.6 cm, *T*=5 cm, *G*=50% and Mo-Rh 29 kVp x-ray spectrum, unless specified otherwise.

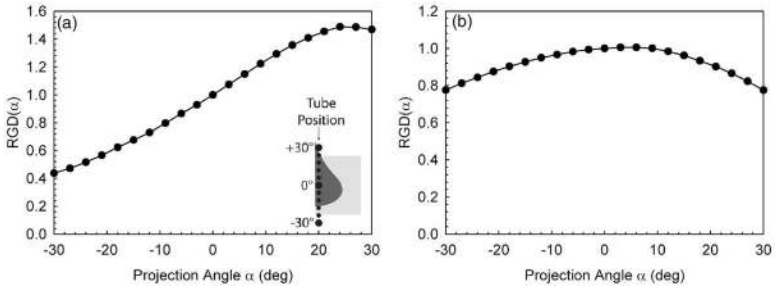

Fig. 10.

Graphs of RGD vs projection angle for (a) CND=7 cm, *T*=8 cm, and (b) CND=19 cm, *T*=8 cm, both for the MLO view.

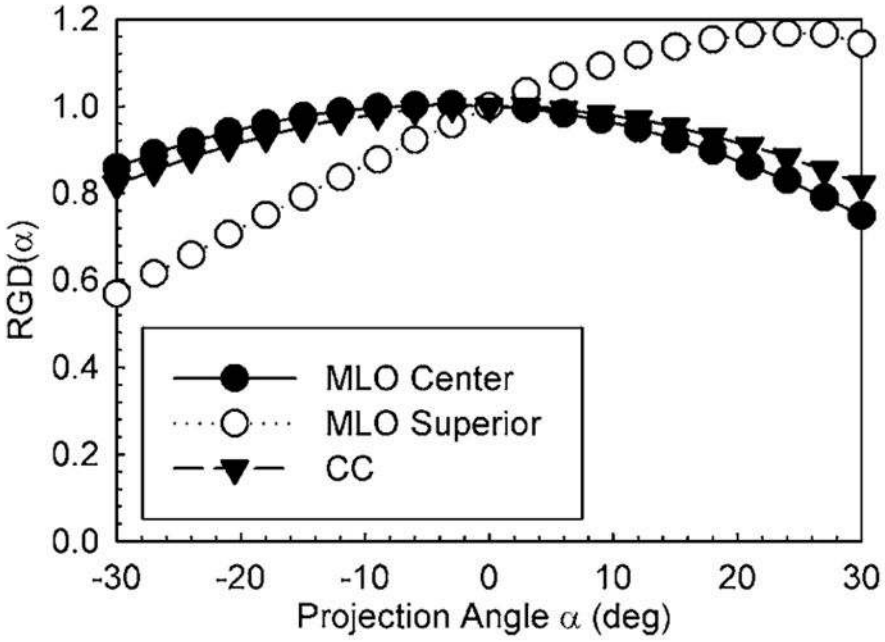

Fig. 11.

Graph of RGD vs projection angle for a small breast in MLO view showing the variation due to placing the breast on the center of the detector rather than towards the superior side. The RGD distribution for the MLO detector-centered breast is compared with the standard MLO view for the same sized breast and with the CC view data for the breast with equivalent mass and thickness.

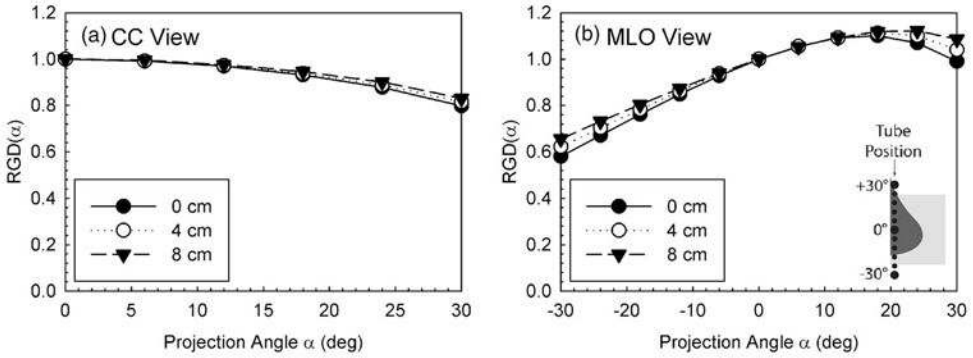

Fig. 12.

Graphs of RGD vs projection angle for three different detector to x-ray tube center of rotation distances. Graph (a) is for a CC view breast with CND=11.6 cm, (b) is for a MLO view breast with CND=13 cm. For both graphs T=8 cm, G=50% and the x-ray spectrum is Mo-Rh 29 kVp.

Table I

First half-value layer values of the x-ray spectra used to combine the mono-energetic Monte Carlo results. The mono-energetic results were combined using the computed HVL above the breast compression plate due to the inclusion of the breast compression plate in the simulation.

Target	Filter	Tube potential (kVp)	Computed HVL above compression plate (mm Al)	Computed HVL under compression plate (mm Al)
Mo	Mo	25	0.284	0.322
Mo	Mo	26	0.297	0.335
Mo	Mo	27	0.309	0.347
Mo	Rh	27	0.364	0.400
Mo	Rh	29	0.387	0.422
Rh	Rh	29	0.380	0.426
Rh	Rh	31	0.408	0.457
Rh	Rh	33	0.435	0.484
Rh	Rh	35	0.459	0.509

Table II

Mean computed normalized glandular dose per unit exposure at the intersection of the central ray and the breast support plate (see Fig. 2) for zero degree projection angle, D_gN_0 (mGy/R). For MLO view data, breasts with a chest-wall to nipple distance of less than 10 cm have a lower D_gN_0 by 6%–14%, for larger breasts the data deviates from the mean reported here by a maximum of 6%. For CC view data, the data deviates from the mean by a maximum of 3%.

		MLO View Glandularity (%)					CC View Glandularity (%)				
Thickness (cm)	**Spectrum (Target/filter/kVp)**	**1**	**25**	**50**	**75**	**100**	**1**	**25**	**50**	**75**	**100**
2	MoMo 25	2.33	2.19	2.05	1.92	1.80	2.59	2.43	2.28	2.13	2.00
	MoMo 26	2.44	2.29	2.14	2.01	1.89	2.70	2.54	2.38	2.23	2.09
	MoMo 27	2.53	2.38	2.23	2.10	1.97	2.81	2.64	2.48	2.33	2.18
	MoRh 27	3.03	2.86	2.69	2.54	2.40	3.34	3.16	2.98	2.81	2.65
	MoRh 29	3.19	3.02	2.85	2.69	2.54	3.52	3.34	3.15	2.97	2.81
	RhRh 29	3.24	3.07	2.91	2.76	2.61	3.57	3.39	3.21	3.04	2.88
	RhRh 31	3.45	3.28	3.11	2.95	2.80	3.79	3.61	3.42	3.25	3.09
	RhRh 33	3.62	3.45	3.28	3.12	2.97	3.98	3.80	3.61	3.43	3.27
	RhRh 35	3.78	3.60	3.43	3.26	3.11	4.15	3.96	3.77	3.59	3.42
3	MoMo 25	1.81	1.65	1.50	1.37	1.25	2.01	1.83	1.66	1.51	1.38
	MoMo 26	1.90	1.73	1.58	1.44	1.32	2.11	1.92	1.75	1.59	1.46
	MoMo 27	1.99	1.81	1.65	1.51	1.38	2.20	2.01	1.83	1.67	1.53
	MoRh 27	2.43	2.23	2.05	1.88	1.73	2.68	2.47	2.26	2.08	1.91
	MoRh 29	2.58	2.37	2.18	2.01	1.85	2.85	2.62	2.41	2.22	2.04
	RhRh 29	2.66	2.46	2.27	2.10	1.95	2.93	2.71	2.50	2.31	2.14
	RhRh 31	2.85	2.65	2.45	2.27	2.11	3.14	2.91	2.70	2.50	2.32
	RhRh 33	3.02	2.81	2.61	2.42	2.25	3.33	3.09	2.87	2.67	2.48
	RhRh 35	3.17	2.95	2.74	2.55	2.38	3.49	3.24	3.02	2.81	2.62
4	MoMo 25	1.45	1.29	1.16	1.04	0.93	1.61	1.44	1.28	1.15	1.03
	MoMo 26	1.53	1.37	1.22	1.10	0.99	1.70	1.52	1.36	1.22	1.09
	MoMo 27	1.60	1.43	1.28	1.15	1.04	1.78	1.59	1.42	1.28	1.15
	MoRh 27	1.99	1.80	1.62	1.46	1.33	2.21	1.99	1.80	1.62	1.47
	MoRh 29	2.12	1.92	1.73	1.57	1.42	2.36	2.13	1.92	1.74	1.58
	RhRh 29	2.22	2.02	1.83	1.67	1.52	2.46	2.24	2.03	1.85	1.68

		MLO View Glandularity (%)					CC View Glandularity (%)				
Thickness (cm)	**Spectrum (Target/filter/kVp)**	**1**	**25**	**50**	**75**	**100**	**1**	**25**	**50**	**75**	**100**
	RhRh 31	2.40	2.19	1.99	1.82	1.66	2.66	2.42	2.20	2.01	1.84
	RhRh 33	2.55	2.33	2.13	1.95	1.78	2.83	2.58	2.36	2.15	1.97
	RhRh 35	2.69	2.46	2.25	2.06	1.89	2.98	2.73	2.49	2.28	2.09
5	MoMo 25	1.20	1.06	0.94	0.83	0.74	1.33	1.17	1.03	0.92	0.82
	MoMo 26	1.27	1.12	0.99	0.88	0.79	1.41	1.24	1.10	0.97	0.87
	MoMo 27	1.34	1.18	1.04	0.93	0.83	1.48	1.31	1.15	1.02	0.91
	MoRh 27	1.68	1.50	1.33	1.19	1.07	1.87	1.66	1.47	1.32	1.18
	MoRh 29	1.80	1.60	1.43	1.28	1.15	2.00	1.78	1.58	1.42	1.27
	RhRh 29	1.90	1.71	1.53	1.38	1.25	2.11	1.89	1.69	1.52	1.38
	RhRh 31	2.06	1.86	1.67	1.51	1.37	2.29	2.06	1.85	1.67	1.51
	RhRh 33	2.21	1.99	1.79	1.62	1.47	2.45	2.21	1.99	1.79	1.63
	RhRh 35	2.33	2.11	1.90	1.72	1.57	2.59	2.34	2.11	1.91	1.73
6	MoMo 25	1.03	0.90	0.79	0.69	0.62	1.13	0.99	0.86	0.76	0.67
	MoMo 26	1.09	0.95	0.83	0.74	0.65	1.20	1.05	0.92	0.81	0.72
	MoMo 27	1.14	1.00	0.88	0.78	0.69	1.26	1.10	0.96	0.85	0.76
	MoRh 27	1.45	1.28	1.13	1.00	0.90	1.61	1.41	1.25	1.10	0.98
	MoRh 29	1.56	1.37	1.21	1.08	0.97	1.73	1.52	1.34	1.19	1.06
	RhRh 29	1.66	1.47	1.31	1.17	1.05	1.84	1.63	1.45	1.29	1.16
	RhRh 31	1.81	1.61	1.43	1.29	1.16	2.00	1.78	1.59	1.42	1.28
	RhRh 33	1.94	1.73	1.55	1.39	1.25	2.15	1.92	1.71	1.53	1.38
	RhRh 35	2.05	1.84	1.64	1.48	1.34	2.28	2.03	1.82	1.63	1.47
7	MoMo 25	0.90	0.78	0.68	0.60	0.53	0.98	0.85	0.74	0.65	0.57
	MoMo 26	0.95	0.83	0.72	0.63	0.56	1.04	0.90	0.79	0.69	0.61
	MoMo 27	1.00	0.87	0.76	0.67	0.59	1.10	0.95	0.83	0.73	0.64
	MoRh 27	1.28	1.12	0.98	0.87	0.77	1.41	1.23	1.08	0.95	0.84
	MoRh 29	1.37	1.20	1.06	0.94	0.83	1.52	1.33	1.16	1.03	0.91
	RhRh 29	1.47	1.30	1.15	1.02	0.91	1.63	1.43	1.26	1.12	1.00
	RhRh 31	1.61	1.42	1.26	1.12	1.01	1.78	1.57	1.39	1.24	1.11
	RhRh 33	1.73	1.53	1.36	1.21	1.09	1.91	1.69	1.50	1.34	1.20
	RhRh 35	1.83	1.63	1.45	1.30	1.16	2.03	1.80	1.60	1.43	1.28

		MLO View Glandularity (%)					CC View Glandularity (%)				
Thickness (cm)	**Spectrum (Target/filter/kVp)**	**1**	**25**	**50**	**75**	**100**	**1**	**25**	**50**	**75**	**100**
8	MoMo 25	0.79	0.69	0.60	0.52	0.46	0.87	0.75	0.65	0.57	0.50
	MoMo 26	0.84	0.73	0.63	0.56	0.49	0.92	0.80	0.69	0.61	0.53
	MoMo 27	0.89	0.77	0.67	0.59	0.52	0.97	0.84	0.73	0.64	0.56
	MoRh 27	1.14	0.99	0.87	0.76	0.68	1.26	1.09	0.95	0.84	0.74
	MoRh 29	1.22	1.07	0.93	0.83	0.73	1.35	1.18	1.03	0.90	0.80
	RhRh 29	1.32	1.16	1.02	0.90	0.81	1.46	1.28	1.12	0.99	0.88
	RhRh 31	1.44	1.27	1.12	0.99	0.89	1.60	1.40	1.24	1.10	0.98
	RhRh 33	1.55	1.37	1.21	1.08	0.96	1.72	1.52	1.34	1.19	1.06
	RhRh 35	1.65	1.46	1.29	1.15	1.03	1.83	1.62	1.43	1.27	1.14

Table III

Sensitivity of the relative glandular dose, RGD(a), to the simulation parameters studied in this work.

		Coefficient of variation		Deviation from mean	
View	**Parameter varied**	**Mean**	**Maximum**	**Mean**	**Maximum**
MLO	Glandularity	0.30%	1.42%	0.40%	1.87%
	X-ray spectrum	0.75%	3.02%	1.01%	4.04%
	Thickness	2.86%	12.35%	4.38%	19.75%
	Chest-wall to nipple distance	10.26%	25.83%	14.49%	37.88%
CC	Glandularity	0.20%	0.84%	0.27%	1.10%
	X-ray spectrum	0.60%	2.09%	0.82%	2.85%
	Thickness	1.00%	4.63%	1.64%	7.15%
	Chest-wall to nipple distance	0.89%	6.40%	1.30%	9.34%

Table IV

Coefficients for the fit Eqs. (3) and (4) to compute relative glandular doses, RGD(a), for both the MLO and CC views.

T (cm)	a	b	c	d	e	f	g	h	i	j	k
MLO view											
2	1.0349358E+00	−1.6529060E-02	1.0077362E-02	6.2692215E-02	5.8595159E-02	5.7527400E-05	−1.7252000E-04	−1.0608000E-03	−9.3921000E-04	8.1035200E-04	−5.6465000E-04
3	9.8285238E-01	−2.2306940E-02	1.0055001E-02	8.4386751E-02	8.7038980E-02	8.2108600E-05	−2.3248000E-04	−1.7703800E-03	−1.8553700E-03	1.1006090E-03	−5.6204000E-04
4	1.0224779E+00	−2.6531450E-02	1.2824346E-02	1.1002425E-01	1.0678169E-01	1.4712400E-04	−2.4763000E-04	−2.6128900E-03	−2.4943400E-03	1.1814080E-03	−8.1818000E-04
5	1.0183296E+00	−2.8581550E-02	1.2678092E-02	9.5063795E-02	9.2354960E-02	1.8802800E-04	−2.3896000E-04	−2.0215100E-03	−1.9115000E-03	1.1423940E-03	−9.3090000E-04
6	9.9363885E-01	−2.8537490E-02	1.4971051E-02	8.6364355E-02	8.7895273E-02	2.4280300E-04	−2.1764000E-04	−1.8136000E-03	−1.8608200E-03	9.0414300E-04	−1.2530800E-03
7	9.6518850E-01	−2.4551700E-02	1.1157589E-02	1.7101855E-02	2.3765749E-02	2.2324400E-04	−1.8127000E-04	8.2918200E-04	5.7414100E-04	6.1190600E-04	−1.1252000E-03
8	9.4728735E-01	−2.0484000E-02	7.9161710E-03	−3.9651870E-02	−3.0315450E-02	1.9929900E-04	−1.4532000E-04	2.9771460E-03	2.6223800E-03	3.6897700E-04	−9.8338000E-04
CC view											
2	9.7671287E-01	−2.8288000E-04	7.0501240E-03	−1.2163000E-04	−6.5277000E-04	−1.0460000E-05	−3.5244000E-07	1.8795400E-05	2.2485200E-06	6.4138300E-08	
3	9.8639604E-01	3.8479100E-04	3.6117490E-03	−1.4252000E-04	−2.6970000E-04	−1.1892000E-04	−2.0850000E-07	5.7938800E-06	7.0957900E-06	−1.2272000E-06	
4	9.8544839E-01	9.0665300E-04	3.4765500E-03	−1.4728000E-04	−2.3755000E-04	−2.2604000E-04	3.2855500E-07	4.5156000E-06	1.2224500E-05	−3.3923000E-06	
5	9.8793549E-01	1.8384160E-03	2.5673120E-03	−1.3668000E-04	−1.3390000E-04	−3.7845000E-04	2.8577900E-07	1.1046500E-06	1.7651900E-05	−4.7866000E-06	
6	9.5957426E-01	2.7563230E-03	1.1131519E-02	−1.2193000E-04	−9.1140000E-04	−5.1403000E-04	2.8172900E-07	2.2933100E-05	2.2262800E-05	−6.5283000E-06	
7	9.2121146E-01	3.8140860E-03	2.1370915E-02	−7.1292000E-05	−1.7795600E-03	−7.2343000E-04	−5.3147000E-07	4.6601600E-05	2.9601500E-05	−8.4001000E-06	
8	8.7176151E-01	4.5144410E-03	3.5520414E-02	−5.5722000E-05	−3.0308200E-03	−8.4009000E-04	−2.3385000E-07	8.1239700E-05	3.4711900E-05	−1.1059000E-05	